arXiv:1703.06466v1 [cond-mat.mtrl-sci] 19 Mar 2017

Adsorption of atoms and molecules on *s*-triazine sheet with embedded manganese atom: First-principles calculations

Yusuf Zuntu Abdullahi[1], Tiem Leong Yoon[2], Mohd Mahadi Halim[3], Md. Roslan Hashim[4], Thong Leng Lim[5], and Kazuhiko Uebayashi[6]

[1]*School of Physics, Universiti Sains Malaysia, 11800 Penang, Malaysia*

[1]*Department of Physics, Faculty of Science, Kaduna State University, P.M.B. 2339 Kaduna State, Nigeria*

[*]*E-mail: yusufzuntu@gmail.com*

[2]*School of Physics, Universiti Sains Malaysia, 11800 Penang, Malaysia*

[*]*E-mail: tlyoon@usm.my*

[3]*School of Physics, Universiti Sains Malaysia, 11800 Penang, Malaysia*

[4]*Institute of Nano-Optoelectronics Research and Technology Laboratory, Universiti Sains Malaysia, 11900 Penang, Malaysia*

[5]*Faculty of Engineering and Technology, Multimedia University, Jalan Ayer Keroh Lama, 75450 Melaka, Malaysia*

[6]*Department of Natural Science, Akita College, National Institute of Technology, Akita 011-8511, Japan*

The mechanical, structural, electronic and magnetic properties of *s*-triazine sheet (C_6N_6) with embedded Mn atom (Mn-C_6N_6) is investigated under the influence of external environment using density functional theory. Our results show that Mn-C_6N_6 system is structurally and mechanically stable. The binding energy of Mn embedded in C_6N_6 sheet can be modulated under the influence of symmetric deformation and perpendicular electric field respectively. The semiconducting property of pure C_6N_6 sheet is maintained upon embedment of Mn atom in the porous site. It is also found that small increment in bi-axial tensile strain enhances the band gap (from 0.630 eV at zero strain to 0.802 eV at 5% strain) while the magnetic moment of the embedded Mn atom is preserved. The electronic and magnetic properties of the Mn-C_6N_6 systems are maintained up to 10 V/nm in electric field strength. We also explore the geometries, electronic and magnetic properties of Mn-C_6N_6 with adsorbed atoms and molecules. The Mn-C_6N_6 with adsorbed O atom and O_2 molecule systems shows half-metallic character whereas the remaining systems preserve their semiconducting property. The total magnetic moment

per unit cell in most of the systems is found to reduce as compared to that of the Mn-C_6N_6 sheet. The reduction in magnetic moment can be related to the strong interactions among the Mn atom and the surrounding atoms which lead to the formation of low-spin configurations. Overall, our results indicate that the Mn-C_6N_6 systems with and without adsorbed atoms and molecules can serve as potential candidates for future spintronics and catalysis applications.

1 Introduction

Research interest in magnetic materials has gained its spectacular boost after the discovery of exotic magnetic properties [1, 2]. Additionally, continued device miniaturization has also opened up many research opportunities to reveal the magnetic properties of these nanostructures in hope for potential applications in spintronics and catalysis. At present, investigations on magnetic nanostructure are directed towards clusters of transition metals (TM). This is due to their large magnetic moments as the dimensionality and coordination (bonds per atom) of the TM cluster are reduced [3, 4]. However, their net magnetic moments can also become decreased, depending on the configuration (ferromagnetic and anti-ferromagnetic geometries) and surrounding of the clusters [5-8]. It is desirable to study the magnetic properties of a TM cluster which is evenly bound to an inert substrate such that the magnetic moment is comparable to that of a cluster in isolation. The interaction of TM atoms with certain metal surfaces is known to be very strong [8,9]. This could potentially affect their net magnetic moments. In contrast, carbon nanostructures are known to be inert, and stand as the right candidate for encapsulation of TM atoms.

Considering two-dimensional carbon nanostructures as substrates, many efforts have been devoted to study the physical and chemical properties of bound TM clusters on graphene [6,7,10] and boron nitride [11,12] sheets. However, previous works have shown that TM atoms bind weakly on graphene and boron nitride monolayers [7,12,13]. Such a weak binding may render TM atoms to diffuse easily on the surface and aggregate to form clusters. Many attempts have been made to create defects in the aforementioned surfaces to prevent the diffusion. However, not much success [12] has been achieved due to technical impracticability to realize controlled defect formation in compacted hexagonal 2D surfaces. Binding of dispersed TM atoms on the surfaces of graphene and other related 2D monolayers presents a practical challenge.

To practically produce controllable nanostructures with desired magnetic properties without altering the physical properties of the bound structures is not technically trivial. Such a challenge has led to the discovery of a new set of graphitic carbon-nitride (CN) sheets [14]. Graphitic CN sheet comes naturally with a regular array of cavities which is wide enough to accommodate any nanostructures that are evenly dispersed. CN sheet has many graphitic allotropes depending on the choice of the primitive unit cell and the C and N atomic coverage in their hexagonal rings. For example, the semiconducting heptazine (t-s-triazine) sheet comprises of 14 C and N atoms in the form of three abreast rings of triazine (consisting of 3 C and 4 N atoms in the unit cell) [15] whereas s-triazine sheet of similar electronic character consists of 12 C and N atoms having two rings of triazines linked together by C-C bond [16].

Both aforementioned allotropes are found to be structurally, energetically and mechanically stable under ambient conditions [15-17].

Having explained the motivation for the choice of graphitic CN sheet over the rest of 2D sheets with compacted hexagonal rings, the embedment of single atoms on the pure graphitic CN sheet has been the most recent interest for many theoretical [18-21] and few experimental [22-25] studies.The structural, electronic and magnetic properties of B, Al, and Cu atoms doped graphitic triazine-based g-C_3N_4 (gt-C_3N_4) systems have been theoretically investigated [26]. Their results have shown that Cu atoms are more stable when situated above the center of the triazine ring. Moreover, they have reported that doping at the interstitial sites leads to thermodynamically stable non-planar structures. It is found that Cu-doped triazine produces a total magnetic moment of 1.0 μB which is mainly localized around p_z like-orbitals of the sheet. The electronic property of Cu-doped triazine systems calculated based on GGA-PBE and HSE06 method exhibits half-metallic behavior. The Cu-doped triazine system has an anti-ferromagnetic ground state. They did not estimate the Curie temperature for Cu-doped triazine system due to the fact that long-range magnetic ordering is usually favorable for the system having ferromagnetic order at zero temperature.

The energetic, electronic, magnetic and optical properties of two-dimensional graphitic carbon nitride (g-C_3N_4) sheets upon embedment of 3d-transition metal (TM) atoms have been investigated by Ghosh *et al.* The g-C_3N_4 sheets with embedded TM atoms are found to be energetically stable when located in the porous sites. It was also reported that the system becomes metallic upon TM (including Cu) embedment. The d orbitals of TMs hybridize with the π-orbitals of the g-C_3N_4 framework and close the band gap in TM-embedded g-C_3N_4 (TM-g-C_3N_4). In most cases the magnetic moment of the 3d TM atoms are well preserved when compared to their isolated values. However, Mn atoms couples antiferromagnetically whereas Cu and Zn atoms are nonmagnetic in the ground state of their corresponding TM-g-C_3N_4 sheets [21]. The claims for magnetic ordering in Mn, Cu embedded g-C_3N_4 sheets and metallic behavior for Cu embedded system at relatively the same separations are in contrast to what was observed by Zhang *et al.* [20] and Meng *et al.* [26] in the same allotropes. In a similar allotrope, Du *et al.* [27] suggest that Mn and Cu atom embedded in C_2N monolayers possess ferromagnetic and paramagnetic ground state respectively when the TM atoms are close to each other, while Meng *et al.* [26] observed antiferromagnetic ground state with half-metallic electronic character for Cu-doped triazine system. In general, the claim for magnetic ordering of TM atoms embedded in CN remains unclear. However, it is feasible to envisage that if the embedded TM atoms were well separated, the possible interactions among themselves could be minimized. The effort to clarify the magnetic ordering issue hence could become less complicated.

More recently, Choudhuri *et al.* [27] investigated newly formed allotrope of the carbon-nitride monolayer (*gt*-C_3N_3) with embedded 3d transition metal atoms (TM@gt-C_3N_3) systems based on density functional theory. It was found that the Cr, Mn and Fe embedded *gt*-C_3N_3 systems are dynamical, thermally and mechanically stable. Moreover, Cr, Mn and Fe embedded in the *gt*-C_3N_3 systems have been found to exhibit high temperature ferromagnetism and high magnetic anisotropy energy (MAE) with a peak value per atom occurring in Cr@*gt*-C_3N_3. Their finding for the ferromagnetic ordering of Mn atom in similar graphitic CN sheet under ambient conditions agrees well with that reported by Du *et al.* [28]. Choudhuri *et al.* [27] further claimed a more enhanced MAE in the presence of an external electric field, an amount far larger than the value computed without electric field.

In our recent studies, it was shown that the band gap of heptazine with embedded Mn atom increases under small biaxial tensile strain whereas the magnetic moment of heptazine with embedded Mn systems remain unperturbed under both tensile strain and applied electric field [18]. It was also observed that the binding energy of heptazine with embedded Mn atom systems decreases as more tensile strain is applied. In contrast, we observed significant increase in binding energy as the strength of electric filed is increased. Modulating binding energy via an applied external field could serve as an effect way to control catalytic process.

Besides spintronics, CN with embedded TM systems can also be utilized for heterogeneous catalysis and in membrane for hydrogen purification from other gases [29-31]. Heterogeneous catalysis based on single atomic crystal (SAC) is the cheapest and easiest way of achieving efficient catalysis. To date, various 2D sheets have been theoretically and experimentally proposed for heterogeneous catalysis [32-37]. Among others, monolayers carbon and related 2D nanostructures, e.g. boron nitride [32,33], graphene [34,35], graphyne [36], silicene [37], carbon nitride sheet [35] have received enormous attentions due to their availability, thermal stability and large surface area. Density functional theory (DFT) calculations have shown that graphene with embedded Au, Fe and Pt [34,38,39] atoms yield good catalytic activity for CO oxidation and oxygen reduction. Experimentally, excellent catalytic activities have been reported for graphene with supported single Pd and Pt using monolayer deposition method [29,40]. Although favorable catalytic process has been reported for SACs of graphene and related 2D materials, the adsorption/binding energies of 3d atoms on their surfaces are relatively weak and could result in formation of cluster that renders reduction in catalytic activity.

2D porous carbon sheets embedded with TM atoms [14,16] are desirable SACs that can serve as membrane for hydrogen purification from other gases [30,31]. This is because they naturally come with regularly array of cavities. These cavities are reported to strongly bind to 3d TM while maintaining structural and electronic features of the sheets [18,21]. A recent

work along this direction has confirmed theoretically that it is possible to synthesize high quality SACs using porous 2D materials with well dispersed 3d TM atoms. More importantly, the 3d TM atoms are found to strongly bind to the C_2N sheet in the cavity without cluster formation, while the intrinsic properties of both porous substrate and the atoms are preserved [41].

In this paper, we are interested to theoretically study the geometries, electronic and magnetic properties of TM-embedded graphitic systems in which different types of atoms and molecules are made to adsorbed onto their surfaces. To be specific, Mn-embedded *s*-triazine will be studied, as well as the adsorption of C, N, O, H atoms and six molecules (CH_4, N_2, O_2, H_2, CO, CO_2) on its surface. *s*-triazine sheet is an allotrope of graphitic carbon nitride which shares some structural similarities with C_2N sheet. It also comes with well separated porous sites which will ensure no interactions between the embedded TM atoms. Mn is chosen instead of other 3d TM species due to its well-ordered spin configurations in the d orbital and desirable characteristics for SAC applications which was reported in previous works.

2 Calculation method

We carried out density functional theory (DFT) [42] calculations using the QUANTUM ESPRESSO code [43]. Generalized gradient approximation (GGA) of Perdew-Burkew-Enzerhof (PBE) [44] and Hubbard U correction [45] (GGA+U) is employed to describe the exchange-correlation energy of strongly localized 3d orbital of Mn atom. Ultrasoft pseudopotentials are used for C, N, and Mn (semi-core included) atoms to account for the core and valence electrons [46]. We employed plain wave basis set with kinetic energy cut-off of 550 eV to expand the wave functions. Marzari-Vanderbilt smearing method with Gaussian spreading is employed [47] to facilitate the convergences of our systems. We used $8\times8\times1$ and $15\times15\times1$ k-point meshes of Brillouin zone (BZ) sampling using the Mankhorst-Pack method for the self-consistent field and density of state calculations respectively [48].

The relaxed structure of 2×2 pure graphitic C_6N_6 sheet (left figure in Fig. 2(a)) consists of 4 units of *s*-triazine (right figure in Fig. 1(a)) with a total of 48 C and N atoms. Each *s*-triazine has two rings of C_3N_3 connected via a C-C bond. The averaged optimized C-C bond length connecting adjacent *s*-triazine unit, C-N bond length and the lattice constant in the pure C_6N_6 are found to be 1.51 Å , 1.34 Å and 14.27 Å respectively (see the left figure in Fig. 1(a)). In the *s*-triazine structure, all C atoms are sp^2-like hybridized whereas N atoms have sp^3-like hybridized structure. Porous site in the graphitic C_6N_6 is encircled by solid line in the left figure in Fig. 1(a). The left figure in Fig 1. (b) shows Mn atom embedded

in the porous site. Henceforth, we shall refer the 2×2 supercell in Fig. 1(a) as C_6N_6, while Mn embedded in C_6N_6 as Mn-C_6N_6 in the left figure of Fig. 1(b). A thick vacuum space of 16 Å along the direction perpendicular to the Mn-C_6N_6 sheet is adopted to avoid the interaction between the periodic sheets. All atoms are fully relaxed until all remaining force on each atom was smaller than 0.05 eV/Å .

As suggested in our previous works [18], inclusion of Hubbard U parameter yield better ground state properties for strongly correlated systems involving TM atoms. We therefore employed linear response approach formulated by Cococcioni *et al.* [45], which is implemented in the PWSCF package [43], to compute the U parameter in this study. In the linear-response scheme calculations, we first evaluated χ_0 and χ which represent the non-interacting (bare) and interacting density response functions of the system with respect to localized perturbations, as illustrated in Fig. 2(a). The parameter U_{eff} is then obtained from the expression: $U_{\text{eff}} = \left(\chi_0^{-1} - \chi^{-1}\right)$. The calculated U_{eff} value for Mn-C_6N_6 is depicted in Fig. 2(a).

3 Results ad Discussions

3.1 Structural and mechanical properties of Mn-C_6N_6 system

Fig. 1(c) displays the relaxed structure of Mn-C_6N_6. The averaged optimized C-C bond length connecting adjacent s-triazine unit and the lattice constant in the Mn-C_6N_6 are found to be 1.48 Å and 14.20 Å respectively. The optimized C-N bond lengths within the porous site are in the range 1.35 - ∼1.37 Å . The calculated values do not deviate much from the un-doped C_6N_6 system and is consistent with that of the previous work [16]. Using strain energy minimization procedures in steps of 0.005 for both uni- and biaxial tensile strains within the linear elastic region (see Fig. 3 and Table 1), mechanical properties are obtained. The elastic constants k_{11}, k_{12}, for uni- and bi-axial strains are 146.90 N/m and 26.20 N/m respectively, which are obtained from Eq. (1). The in-plane stiffness (Young modulus), and poison ration can be deduced from Eq. (2). These equations are expressed as:

$$\begin{aligned} k_{11} &= \frac{1}{A_0}\left[\frac{\partial^2 U}{\partial s^2}\right]_{s=0} \quad \text{(uniaxial)} \\ 2(k_{11}+k_{12}) &= \frac{1}{A_0}\left[\frac{\partial^2 U}{\partial s^2}\right]_{s=0} \quad \text{(bi-axial)} \end{aligned} \tag{1}$$

In-plane stiffness and Poisson's ratio:

$$\begin{aligned} Y &= k_{11}(1-\nu^2), \\ \nu &= \frac{k_{12}}{k_{11}} \end{aligned} \tag{2}$$

where k_{11}, k_{22} denote elastic constants, A_0, U, and s are equilibrium unit-cell area, strain energy and applied tensile strain. The computed in-plane stiffness and Poisson's ratio are 1421.4 GPa·Å (= 142.14 N/m) and 0.18 respectively. This shows that Mn-C_6N_6 is less stiff than heptazine [15] and graphyne sheets [48]. The decreased in stiffness in comparison with heptazine can be linked to a weaker bonding of the hexagonal rings of the sheet. Moreover, the calculated Poisson's ratio is slightly larger than the value for graphene [50]. To evaluate the bulk modulus, we use second derivative of the bi-axial strain energy as a function of area of the Mn-C_6N_6 sheet, which is expressed as

$$G = A \times \left(\frac{\partial^2 U}{\partial A^2}\right)\Big|_{A_m} \tag{3}$$

where A, U and A_{m} denote the area of the Mn-C_6N_6 sheet, the bi-axial strain energy and the equilibrium area of Mn-C_6N_6 respectively. Fig. 3 iii shows the bi-axial strain energy as a function of the area of Mn-C_6N_6 sheet. The computed value for the bulk modulus of Mn-C_6N_6 sheet is 86.49 N/m which is also lower than the value for Mn embedded in heptazine sheet [18]. The lowering of the value for bulk modulus can also be related to the compact hexagonal rings within the heptazine sheet as compared to separated rings in s-triazine sheet. All the computed results of elastic constants confirm that Mn-C_6N_6 is mechanically stable.

To further examine the structural stability of Mn-C_6N_6, the averaged bond lengths $d_{\text{Mn-N}}$ between the embedded Mn and six nearest neighbor N atoms in the porous site, the averaged bond lengths d connecting adjacent s-triazine, and h the height of the Mn atom with respect to the Mn-C_6N_6 plane for strained and unstrained systems are listed in Table 2. We have also checked the binding energy of Mn in the Mn-C_6N_6 sheet as a function of bi-axial tensile strain for the range of 0-6%. The binding energy of the Mn-C_6N_6 is calculated as

$$E_b = (E_{\mathrm{C_6N_6}} + E_{\mathrm{Mn}}) - E_T \tag{4}$$

where E_T is the total energy of Mn-C_6N_6 sheet, $E_{\mathrm{C_6N_6}}$ represents the energy of pristine C_6N_6 sheet, and E_{Mn} is the total energy of an isolated Mn atom. Positive binding energy is an indication of a stable structure. According to Eq. (4), the unstrained Mn-C_6N_6 has a binding energy of 4.14 eV, which is roughly the same as that obtained in the recent works [41,51]. As can be seen in Table 2, there is little difference in the predictions of structural and magnetic

properties of unstrained Mn-C_6N_6 calculated in this work as compared to previous results. Here we state clearly the differences in terms of methodology and the choice of the unit cell between our calculations and the previous works. While we consider DFT+U calculations in our Mn-C_6N_6 system, the work in Ref. [51] employed only DFT without Hubbard U in the presumably same system. We opine that accurate computation of geometries and electronic properties in a system involving strongly correlated atoms can only be achieved if Hubbard U is included [45]. The main difference between the present work and that of Ref. [41] lies within the choice of the unit cell. We use allotrope of graphitic carbon nitride (CN) sheet with equal number of C and N in all the hexagonal rings, with two rings connected via C-C bond in the unit cell with no dangling bond, whereas Ref. [41] used different allotrope of graphitic CN sheet. We anticipate that our results should agree with theirs since the environment where Mn atom is placed is probably the same.

We have further investigated the energetic, structural, electronic and magnetic properties under uniform tensile strain from 0% to 6%. For increasing tensile strain, the calculated value of the Mn height h in the optimized Mn-C_6N_6 plane confirms the planarity of the sheet, where only slight movement of the Mn within the plane was found. We also observed that as the applied tensile strain increases the binding energy of Mn in the porous site becomes less pronounced. The decrease of the binding energy can be understood as follows. In general, elastic energy, U, for small deformations is positive. It is proportional to the product of square of the strain and the elastic module(s) related to biaxial tensile strain, which is (are) supposed to be positive as well. So for positive elastic moduli, the total energy (which is negative in value) of the Mn-C_6N_6 system should increase under small strain. Consequently, the binding energy (which is positive in value), according to the definition of Eq. (4), would become lower. We observe a uniform increase in the average C-C bond lengths connecting the heptazine units. Additionally, it was found that the average bond lengths between the embedded Mn and six nearest neighbor N atoms in the porous site increase accordingly as well. Overall, the decrease in the binding energy is due to structural distortion. At a 6% tensile strain, metastable structure is formed in which the binding energy, E_b, becomes negative (see Table 2)

3.2 Electronic and magnetic properties Mn-C_6N_6

Our calculations show that Mn embedded in C_6N_6 maintains its isolated magnetic moment for both strained and unstrained systems. This indicates that the magnetic moment is less sensitive to the applied bi-axial tensile strain. The corresponding magnetic moments for various systems are listed in Table 2, and the magnetic moment for unstrained Mn-C_6N_6 system agrees well with the previous literatures [41,51]. We can as well observe from the

magnetic moments per atom in Table 2 that the magnetism of Mn-C_6N_6 systems is mainly contributed by the Mn atom. Lowdin's charge analysis shows that electron redistribution of Mn orbitals are mainly from s, p orbitals of Mn whereas d orbital relatively retain its unpaired electrons (high-spin configuration is maintained in each deformation It is found that charge transfer into the C_6N_6 sheet, Q, which is calculated from Lowdin's charge analysis, is relatively maintained in all deformations.

The coupling (i.e., ionic interaction between the Mn atom and C_6N_6 sheet) does not decrease the number of spin-polarized d orbital electrons of Mn atom. We also show the top view plot of the charge-density difference between the Mn atom and the surrounding C and N atoms of strain-free system in the right figure of Fig. 1(b). The figure indicates charge localization around the most electronegative N edge (dotted black color) atoms in the porous site. The charge depletion between the atoms confirms the covalent property of the bonds [52].

The total density of state (TDOS) of pure C_6N_6 is illustrated in Fig. 2(b). The pure C_6N_6 is a direct band gap semiconductor with a band gap of approximately 1.53 eV. The calculated bang gap tallies well with the previous work [16]. The embedment of Mn atom into the C_6N_6 induces magnetism for Mn-C_6N_6 system while maintaining the intrinsic electronic property of the C_6N_6 sheet. This is evident by comparing Fig. 2(c) (which shows the TDOS of the pure C_6N_6 sheet) and Figs. 4 (a)-(c) (which shows the spin-polarized TDOS for the strain-free Mn-C_6N_6 system). The asymmetric TDOS of Mn-C_6N_6 system confirms the presence of magnetic moment in the system.

The spin-polarized projected density of state (PDOS) in Figs. 4 (d)i - (f)i, illustrate the atomic orbital contributions of Mn-C_6N_6 system to valence and conduction bands around Fermi level. The 6 edge N atoms in the porous site formed bonds with the embedded Mn atom. In the plane of C_6N_6, the lone pairs of N atoms face the d_{xy} and $d_{x^2-y^2}$ orbitals of Mn atom. Due to repulsive effect between the p_x, p_y orbitals of N atom and the d_{xy}, $d_{x^2-y^2}$ orbitals of Mn atom, the p_z orbital will be at higher energy. Additional evidence can be referred to Fig. 4(d) which shows that the bottom of the conduction band is dominated by p_z-like orbitals of the six edge N atoms in both spin states, whereas the other orbitals (e.g., s, p_x, p_y) are located in the valence band (which is at a lower energy). This is supported by the measured EC values as shown in Table 2, where these values increase with increasing tensile strain. Moreover, the top of valence band displays dominance by lone pairs of N atoms. The remnant d-like orbitals would be forced to the lower energies. At approximately -6.5 eV and -8.0 eV the bonding orbitals are mainly due to sp-like orbitals of the edge N atoms, and s-, p_x- and d-like orbitals of the Mn atom. Around -4.5 eV there is a hybridization which is occupied by s-, d_{zx}- and d_{z^2}- like orbitals of the Mn atom, as well as sp-like orbitals

of the edge N atoms in the minority spin state. The sp-like orbitals of the Mn atom in both spin up and spin down channels portray intra-orbitals electron transfer.

We also observe band gap modulation of Mn-C_6N_6 under uniform deformation. Small increment in the band gap when bi-axial tensile strain is applied can be explained as follows. From the PDOS Figs. 4 (d)ii-(f)ii of strained Mn-C_6N_6 sheet (3% bi-axial tensile strain), we observe a uniform shift of p_z-like states towards higher energy and backward shift of lone pairs of N edge atoms as larger bi-axial tensile strain is applied. This results in band gap increase. We note that the symmetric deformation causes the lone pairs to become misaligned, thereby causing p_z-like orbital to shift towards higher energy so as to reduce the steric repulsions between the p_x, p_y orbitals of N atom and the $d_{xy}, d_{x^2-y^2}$ orbitals of Mn atom.

3.3 Electric field effect

To study more effects of external environment on the Mn-C_6N_6 sheet, we have perturbed the Mn-C_6N_6 system with an applied perpendicular electric field ranging from 0.0 to 10 V/nm. Under each applied electric field strength, the Mn-C_6N_6 system was fully-optimized. The Mn-C_6N_6 system slightly buckles after optimization. The buckling becomes more prominent at the maximum value of 10 V/nm (bottom figure in Fig. 1(b)). Related to the buckling, the binding energy calculated at each applied electric field strength shows an increasing pattern (see Fig. 2(b)). This indicates that the larger the applied electric field is, the stronger the binding of Mn atom in the porous site becomes. It is expected that the semiconducting property of Mn-C_6N_6 system would change under the application of electric fields, as reported for some related 2D materials [53]. However, despite the small wrinkles, the electronic and magnetic properties of Mn-C_6N_6 are retained up to a peak value of 10 V/nm. To show that the semiconducting property remains unchanged, we have plotted the TDOS of Mn-C_6N_6 at a maximum of 10 V/nm (see Fig. 2 (d)). This can be obviously seen by comparing Fig. 2(d) and Fig. 4 (c). Specifically, the semiconducting property remains unchanged.

The appearance of wrinkles in the Mn- C_6N_6 under applied electric field is due to distortion caused by d_{xy}, $d_{x^2-y^2}$ orbitals of Mn in trying to lower the system's energy. As a result, the hexagonal structure is distorted. We refer to the projected density of states plots (see Figs. 4 (d)-(f)) where we show the orbital hybridizations between p_x, p_y orbitals of N and d_{xy}, $d_{x^2-y^2}$ of Mn. This clearly indicates that both the orbitals are on the same plane. Due to repulsion between the orbitals, the system energy becomes lower. These conditions of having preserved electronic and magnetic properties under applied electric field of Mn-C_6N_6 sheet could be used in future nano-devices.

3.4 Adsorption of atoms on Mn C_6N_6sheet

We first relaxed the Mn-C_6N_6 with each type of atoms (C, N, O, H) adsorbed at a height of 2 Å above Mn atom in the sheet. We do not impose any geometry constraint during structural relaxation. After relaxation, the Mn-C_6N_6 sheets remain planar with no sign of wrinkles in the structures (see Figs. 5 (i)-(iv). The optimized structural properties and corresponding adsorption energies are listed in Table 3. We find that the calculated optimized bond length between the embedded Mn atom and the adsorbed atoms, $d_{\mathrm{Mn}-X}$ (Xstands for atoms or molecules), varies only slightly in the range 1.70-1.92 Å . This range of value confirms the expected covalent bond length between the Mn and the adatoms (adsorbed atoms). To quantify the extent of chemisorption of the adsorbates on Mn-C_6N_6 sheet, we compute their adsorption energies defined in the Eq. (5) below,

$$E_{\mathrm{ads}} = (E_{\mathrm{Mn}-\mathrm{C_6N_6}} + E_X) - E_T \tag{5}$$

where E_T is the total energy of Mn-C_6N_6 with adsorbates, $E_{\mathrm{Mn}-\mathrm{C_6N_6}}$ represents the energy of Mn-C_6N_6 system, and E_{X} is the total energy of an isolated atom or molecules. Positive adsorption energy shows a stable structure. As illustrated in Table 3, N atom has the lowest adsorption energy and the weakest covalent bond length. This can be related to the nature of interaction between the Mn and N atom, in which nitrogen is the most electronegative among the adatoms. In general, the adsorption energies and their corresponding bond lengths show that the structures are stable and all atoms are chemically bonded to the embedded Mn atom in the C_6N_6 sheet.

The total magnetic moment per unit cell and per atom are also shown in Table 3. Unlike the Mn-C_6N_6 system, the magnetic moment per unit cell are found to be reduced when atoms are adsorbed on the Mn-C_6N_6 sheet. The order of magnetic moment of Mn-C_6N_6 with adatoms is C>N>O>H. As can be seen in Table 3, magnetism is mainly contributed by the Mn atom, and the adatoms couple antiferromagnetically with the embedded Mn atom. To clarify the reason for reduction in total magnetic moment per unit cell, we have evaluated the charge transfer into the C_6N_6 sheet and adatoms in the structure. It can be clearly seen that the reduction is a consequence of electron injection into the C_6N_6 sheet from the adatoms and Mn. Such an electron redistribution between the orbitals of Mn and the surrounding atoms induces strong interaction. The interaction reduces the number of spin-polarized electrons of Mn atom. Consequently, these low-spin configurations lead to the reduction of the system's total magnetic moment. The TDOS of Mn-C_6N_6 with adsorbed atoms are depicted in Fig. 5. In spite of hybridization between the adatoms and the embedded Mn atom, the electronic structures of the majority of the systems remain semiconducting

with their respective band gaps listed in Table 3. The TDOS for Mn-C_6N_6 with adsorbed O atom shows half metallic electronic character.

3.5 Adsorption of molecules on Mn-C_6N_6 sheet

Six molecules (CH_4, N_2, O_2, H_2, CO, CO_2) adsorbed at a height of 2 Å above the porous sites in the Mn-C_6N_6 sheet are considered. We do not impose any geometry constraint during structural relaxation. As depicted in Fig. 6 (i) – (vi), the Mn-C_6N_6 sheet remains planar with no sign of buckling in the structure after relaxation. The optimized bond length between the embedded Mn atom and the nearest atom in the adsorbed molecules $d_{\mathrm{Mn}-X}$ are in the range 2.1-2.6 Å and the adsorption energies are in the range of 0.11 - ˜ 0.76 eV. The optimized bond lengths for isolated molecules in all cases, except oxygen, are maintained after adsorption. Based on the previous report [41], the interaction between embedded 3d TM and O_2 is usually strong; we have confirmed this assertion for the embedded Mn atom with adsorbed O_2. We note that Mn-C_6N_6 with adsorbed O_2 has the highest adsorption energy and lowest optimized bond length, $d_{\mathrm{Mn}-\mathrm{O}_2}$, due to strong chemisorption. The bond length of the isolated O_2 is slightly lower than the bond length of the adsorbed O_2. This finding is consistent with the previous work [41].

Interestingly, $d_{\mathrm{Mn}-\mathrm{CO}}$ is the largest among all $d_{\mathrm{Mn}-X}$, showing that CO is the weakest of all molecules that bind to the surface., Correspondingly, its adsorption energy is also low. The weak chemisorption energy for CO confirms the previously reported assertion that O_2 would preferentially cover the Mn-C_6N_6 as compared to CO when the two gases are simultaneously released at constant pressure on the surface [41]. Their conclusion was reached based on the calculation that assumes O_2 has larger adsorption energy as compared to that of CO molecule. Here we would like to contribute to the understanding of adsorption of O_2 and CO based on our previous computations of binding energies of Mn-C_6N_6 systems under bi-axial tensile strain and applied perpendicular electric field. The binding energy is found to reduce under symmetric deformation induced by bi-axial tensile strain, and increase as larger electric field strength is applied. Therefore, these external environments can be used to modulate the adsorption energy. For example, the adsorption energy for O_2 shows decreasing pattern from 0.789 eV @ 0.5% to 0.658 @ 1% as larger symmetric deformations (biaxial tensile strain) are applied. Correspondingly, adsorption energy of CO on Mn-C_6N_6 becomes larger from 0.189 eV @ 1 V/nm to 0.243 @ 2 V/nm as larger electric field strengths are applied. We hope that the two methods of modulating the adsorption energy could be useful in the single crystal field (SAC) application.

The adsorption energies for CH_4, N_2, H_2 molecules on Mn-C_6N_6 are in agreement with recent adsorption energies reported for the same molecules adsorbed on pure C_6N_6 [54].

However, due to interactions between the embedded Mn atom and the molecules, the corresponding $d_{\mathrm{Mn}-X}$ are found to be lower. Our calculated adsorption energy for CO_2 is within the value suggested by Deng *et al.* [55], and the molecule is slightly physisorbed on Mn-C_6N_6 sheet.

The total magnetic moments per unit cell for molecular adsorption on Mn-C_6N_6 are comparable to Mn-C_6N_6 except for the O_2 molecule. As for previous cases, this observation can be explained in terms of electron redistribution between the orbitals in Mn atom and the surrounding atoms (O adatoms included) induced by strong interaction among themselves. This causes the number of spin-polarized electrons of Mn atom to become reduced. The consequent low-spin configurations resulted from reduction in number of unpaired electron renders the total magnetic moment to reduce. We have also calculated the charge transfer into the C_6N_6 sheet and adatoms in the structure. It is evident that the reduced unpaired electrons are resulted from the electron injection into the C_6N_6 sheet and the adatoms from Mn atom. The TDOS of Mn-C_6N_6 with adsorbed molecules are shown in Fig. 6 (i) – (vi). Except Mn-C_6N_6 with adsorbed O_2 molecule showing half metallic character, all the remaining systems have their semiconducting electronic structure maintained. The band gaps are listed in Table 3.

4 Conclusions

In this work, mechanical, structural, electronic and magnetic properties of C_6N_6 with embedded Mn atom is studied systematically under the influence of external environment using density functional theory calculation. The Mn-C_6N_6 is found to be structurally and mechanically stable. Our results show that the binding energy of Mn embedded in C_6N_6 decrease as larger tensile strain is applied. The decrease in binding energy can be related to the structural distortion of the C_6N_6 sheet. We find that the semiconducting property of the pure sheet is preserved after the embedment of Mn atom in porous site. We have shown a linear relation in the increment of band gap and applied bi-axial tensile strain imposed on the Mn-C_6N_6 systems. Magnetic moment of the embedded Mn atom is preserved in all cases. Additionally, Mn-C_6N_6 sheet slightly buckles after structural relaxation under the influence of applied perpendicular electric field. Despite the obvious wrinkles in the Mn-C_6N_6 structure, the electronic and magnetic properties of the Mn-C_6N_6 systems are maintained up to a peak value of 10 V/nm in electric field strength. We also investigate the geometries, electronic and magnetic properties of Mn-C_6N_6 with adsorbed atoms and molecules. Except for Mn-C_6N_6 with adsorbed oxygen atom and molecule which show half metallic character, the remaining systems maintained the semiconducting property of the Mn-C_6N_6 sheet. The

total magnetic moment per unit cell in most of the systems is found to reduce as compared to that for Mn-C_6N_6 sheet. The reduction in magnetic moment can be related to the strong interactions among the Mn atom and the surrounding atoms which lead to the formation of low-spin configurations. In general, these results indicate that Mn-C_6N_6 systems with and without adsorbed atoms and molecules can serve as potential candidates for future spintronics and catalysis applications.

Acknowledgments

T. L. Yoon wishes to acknowledge the support of Universiti Sains Malaysia RU grant (No. 1001/PFIZIK/811240). Figures showing atomic model and 2D charge-density difference plots are generated using the XCRYSDEN program Ref. [56]. We gladfully acknowledge Dr. Chan Huah Yong from the School of Computer Science, USM, for providing us computing resources to carry out part of the calculations done in this paper.

References

[1] M.N. Baibich, J.M. Broto, A. Fert, F.N. Van Dau, F. Petroff, P. Etienne, G. Creuzet, A. Friederich, J. Chazelas, Phys. Rev. Lett., 61 (1988) 2472.

[2] G. Binasch, P. Grunberg, F. Saurenbach, W. Zinn, Phys. Rev. B., 39 (1989) 4828.

[3] Rollmann, G., Sahoo, S., Hucht, A., & Entel, P. Phys. Rev. B., 78 (2008) 134404.

[4] Zeleny, M., Šob, M., & Hafner, J. Phys. Rev. B., 80 (2009) 144414.

[5] D. Duffy, J. Blackman, Phys. Rev. B., 58 (1998) 7443.

[6] Y.Z. Abdullahi, M. Rahman, S. Abubakar, H. Setiyanto, Quantum Matter, 4 (2015) 430.

[7] M. Rahman, Y.Z. Abdullahi, A. Shuaibu, S. Abubakar, H. Zainuddin, R. Muhida, H. Setiyanto, J. Comput. Theor. Nanosci., 12 (2015) 1995.

[8] V. Stepanyuk, W. Hergert, K. Wildberger, R. Zeller, P. Dederichs, Phys. Rev. B., 53 (1996) 2121.

[9] B. Lazarovits, L. Szunyogh, P. Weinberger, Phys. Rev. B., 65 (2002) 104441.

[10] A. AlZahrani, Physica B Condens Matter., 407 (2012) 992.

[11] Y.Z. Abdullahi, M.M. Rahman, A. Shuaibu, S. Abubakar, H. Zainuddin, R. Muhida, H. Setiyanto, Physica B Condens Matter., 447 (2014) 65.

[12] Z. Zhang, Z. Geng, D. Cai, T. Pan, Y. Chen, L. Dong, T. Zhou, Physica E., 65 (2015) 24.

[13] Y. Yagi, T.M. Briere, M.H. Sluiter, V. Kumar, A.A. Farajian, Y. Kawazoe, Phys. Rev. B., 69 (2004) 075414.

[14] E. Kroke, M. Schwarz, E. Horath-Bordon, P. Kroll, B. Noll, A.D. Norman, New J. Chem., 26 (2002) 508.

[15] Y. Z. Abdullahi, T. L. Yoon, M. M. Halim, M. R. Hashim, T. L. Lim, Solid State Commun., 248 (2016) 144.

[16] A. Wang, X. Zhang, M. Zhao, Nanoscale 6 (2014) 11157.

[17] D.M. Teter, R.J. Hemley, Science 271 (1996) 53.

[18] Y.Z. Abdullahi, T.L. Yoon, M.M. Halim, M.R. Hashim, M.Z.M. Jafri, L.T. Leng, Curr. Appl. Phys., 16 (2016) 809.

[19] S.M. Aspera, H. Kasai, H. Kawai, Surf. Sci., 606 (2012) 892.

[20] S. Zhang, R. Chi, C. Li, Y. Jia, Phys. Lett. A., 380 (2016) 1373.

[21] D. Ghosh, G. Periyasamy, B. Pandey, S.K. Pati, J. Mater. Chem. C., 2 (2014) 7943.

[22] J. Tian, Q. Liu, A.M. Asiri, A.O. Al-Youbi, X. Sun, Anal. Chem., 85 (2013) 5595.

[23] P. Niu, L. Zhang, G. Liu, H.M. Cheng, Adv. Funct. Mater., 22 (2012) 4763.

[24] N. Fechler, G.A. Tiruye, R. Marcilla, M. Antonietti, RSC Adv., 4 (2014) 26981.

[25] K. Sridharan, P. Sreekanth, T.J. Park, R. Philip, J. Phys. Chem. C., 119 (2015) 16314.

[26] B. Meng, W.-z. Xiao, L.-l. Wang, L. Yue, S. Zhang, H.-y. Zhang, Phys. Chem. Chem. Phys., 17 (2015) 22136.

[27] I. Choudhuri, P. Garg, B. Pathak, J. Mater. Chem. C., 4 (2016) 8253.

[28] J. Du, C. Xia, W. Xiong, X. Zhao, T. Wang, Y. Jia, Phys. Chem. Chem. Phys., 18 (2016) 22678.

[29] S. Sun, G. Zhang, N. Gauquelin, N. Chen, J. Zhou, S. Yang, W. Chen, X. Meng, D. Geng, M.N. Banis, Sci. Rep., 3 (2013).

[30] Y. Ji, H. Dong, H. Lin, L. Zhang, T. Hou, Y. Li, RSC Adv., 6 (2016) 52377.

[31] Z. Ma, X. Zhao, Q. Tang, Z. Zhou, Int. J. Hydrogen Energy., 39 (2014) 5037.

[32] X. Liu, T. Duan, Y. Sui, C. Meng, Y. Han, RSC Adv., 4 (2014) 38750.

[33] S. Sinthika, E.M. Kumar, R. Thapa, J. Mater. Chem. A., 2 (2014) 12812.

[34] S. Stolbov, M. Alcantara Ortigoza, J. Chem. Phys., 142 (2015) 154703.

[35] G. Vile, D. Albani, M. Nachtegaal, Z. Chen, D. Dontsova, M. Antonietti, N. Lopez, J. Perez-Ramirez, Angew. Chem. Int. Ed., 54 (2015) 11265.

[36] P. Wu, P. Du, H. Zhang, C. Cai, Phys. Chem. Chem. Phys., 17 (2015) 1441.

[37] F. Ersan, O. Arslanalp, G. Gokoglu, E. Akturk, Appl. Surf. Sci., 371 (2016) 314.

[38] Y. Li, Z. Zhou, G. Yu, W. Chen, Z. Chen, J. Phys. Chem. C., 114 (2010) 6250.

[39] Y. Tang, Z. Yang, X. Dai, Phys. Chem. Chem. Phys., 14 (2012) 16566.

[40] H. Yan, H. Cheng, H. Yi, Y. Lin, T. Yao, C. Wang, J. Li, S. Wei, J. Lu, J. Am. Chem. Soc., 137 (2015) 10484.

[41] D. Ma, Q. Wang, X. Yan, X. Zhang, C. He, D. Zhou, Y. Tang, Z. Lu, Z. Yang, Carbon 105 (2016) 463.

[42] P. Hohenberg, W. Kohn, Phys Rev., 136 (1964) B864.

[43] P. Giannozzi, S. Baroni, N. Bonini, M. Calandra, R. Car, C. Cavazzoni, D. Ceresoli, G.L. Chiarotti, M. Cococcioni, I. Dabo, J. Phys. Condens. Matter., 21 (2009) 395502.

[44] J.P. Perdew, K. Burke, M. Ernzerhof, Phys. Rev. Lett., 77 (1996) 3865.

[45] M. Cococcioni, S. De Gironcoli, Phys. Rev. B., 71 (2005) 035105.

[46] D. Vanderbilt, Phys. Rev. B., 41 (1990) 7892.

[47] D. Vanderbilt, Phys. Rev. B., 41 (1990) 7892.

[48] H.J. Monkhorst, J.D. Pack, Phys. Rev. B., 13 (1976) 5188.

[49] M. Asadpour, S. Malakpour, M. Faghihnasiri, B. Taghipour, Solid State Commun., 212, 46 (2015).

[50] E. Cadelano, P.L. Palla, S. Giordano, L. Colombo, Phys. Rev. B., 82 (2010) 235414.

[51] K. Srinivasu, B. Modak, S.K. Ghosh, Phys. Chem. Chem. Phys., 18 (2016) 26466.

[52] P.O. Lowdin, J. Chem. Phys., 18 (1950) 365.

[53] B. Huang, H. Xiang, J. Yu, S.-H. Wei, Phys. Rev. Lett., 108 (2012) 206802.

[54] Ma, Z., Zhao, X., Tang, Q., & Zhou, Z, Int. J. Hydrogen Energy., 39 (2014) 5037-5042.

[55] Q. Deng, L. Zhao, X. Gao, M. Zhang, Y. Luo, Y. Zhao, Small 9 (2013) 3506.

[56] A. Kokalj, Computer. Mater. Sci., 28 (2003) 155.

*

Table 1 Optimized lattice parameters and total strain energy of Mn-C_6N_6 system for mechanical properties computation.

Strain (%)	Area (Å ^{2})	Total energy Biaxial (Ry)	Total energy Uniaxial (Ry)	Lattice parameter Biaxial (Å)
-0.02	167.61	-959.07561	-959.10937	13.12/24.10
-0.015	169.32	-959.10183	-959.12084	13.98/24.22
-0.01	171.05	-959.12023	-959.12875	14.05/24.34
-0.005	172.78	-959.13109	-959.13287	14.13/24.47
0	174.52	-959.13465	-959.13465	14.20/24.59
0.005	176.27	-959.13151	-959.13342	14.27/24.71
0.01	178.03	-959.12150	-959.12937	14.34/24.83
0.015	179.79	-959.10532	-959.12240	14.41/24.96
0.02	181.57	-959.08281	-959.11258	14.48/25.08

Table 2 Geometry and electronic structure for strained/unstrained Mn-C_6N_6. The binding energies E_b, the average bond length between Mn atom and N_{edge} atoms, average bond length connecting the *s*-triazine, and Mn height are respectively named as $d_{\text{Fe-N}}$, d_1/d_2, and h (is the difference in the z-coordinate of the Mn atom and the average of the z-coordinate of all the C and N atoms in the C_6N_6 sheet). Charge transfer, magnetic moment per unit cell and per Mn atom,electronic character of the Mn-C_6N_6system are denoted by Q, M_{cell}, M_{Fe}, EC respectively. All the systems are semiconducting, Values in the EC column denotes that of the semiconducting band gap.

Strain	E_b (eV)	$d_{\text{Mn-N}}$ (Å)	d (Å)	H (Å)	Q (electrons)	M_{Mn} (μ_B)	M_{cell} (μ_B)	EC
0%	4.14	2.70	1.48	-0.011	0.75	5.00	5.02	0.630
1%	3.97	2.75	1.50	-0.007	0.75	5.01	5.02	0.660
2%	3.44	2.79	1.52	0.003	0.76	5.02	5.02	0.675
3%	2.60	2.84	1.55	0.010	0.76	5.00	5.03	0.764
4%	1.48	2.89	1.58	0.014	0.77	5.04	5.04	0.807
5%	0.10	2.93	1.60	0.000	0.77	5.06	5.05	0.802
6%	-1.49	2.99	1.63	0.003	0.77	5.09	5.07	0.952

Table 3 Geometry and electronic structure for Mn-C_6N_6 with adsorbed atoms/molecules. X refers to an adsorbate species. E_{ads} refers to adsorption energy, $d_{\mathrm{Mn}-X}$ refers to averaged bond length between Mn atom and the adsorbates. d_{avg-X} refers to bond length of molecules. The values without parenthesis are that for absorbed molecules while that in parenthesis are for isolated molecules. Q refers to net charge transfer among the adsorbates and the Mn-C_6N_6 sheet. The values without parenthesis are charge transfer from Mn atom into the sheet or adsorbates. These values are all positive as electron from Mn atom always get transferred into the surrounding. The Q values in parenthesis are charge transfer into the Mn-C_6N_6 sheet from adsorbates. Positive values mean electron is transferred into the surroundings (Mn-C_6N_6 sheet) from adsorbates, and vice versa. M_{cell} refers to magnetic moment per unit cell. M_{atom} refers to magnetic moment of Mn atom or adsorbates. The values without parenthesis are that for Mn atom, while that in parenthesis are that for the adsorbates. EC refers to the electronic character of the Mn-C_6N_6 with adsorbates. In the present case, EC can be either half metallic (HM) or semiconducting (SC). The values in the SC case are that of its corresponding band gap.

System	E_{ads} (eV)	$d_{\mathrm{Mn\text{-}X}}$ (Å)	$d_{avg\text{-}X}$ (Å)	Q (electrons)	$\mathrm{M_{cell}}$ (μ_{B})	$\mathrm{M_{atom}}$ (μ_{B})	EC
C	1.98	1.91	-	0.40 (0.13)	2.25	4.56 (-2.25)	SC (0.843)
N	1.37	2.54	-	0.58 (0.18)	2.68	4.76 (-2.11)	SC (0.440)
O	2.53	1.89	-	0.65 (0.41)	3.89	4.83 (-0.98)	HM
H	1.51	1.70	-	0.48 (0.16)	4.78	4.92 (-0.20)	SC (0.900)
CO	0.16	2.66	1.14 (1.15)	0.67 (C: -0.30, O: 0.07)	5.00	4.98 (0.00)	SC (0.793)
CO_2	0.35	2.40	1.18 (1.18)	0.69 (C: -0.79, O: -0.43)	5.00	4.97 (0.00)	SC (0.822)
O_2	0.76	2.12	1.23 (1.32)	0.66 (0.20)	3.48	4.90 (-1.43)	HM
N_2	0.11	2.54	1.12 (1.11)	0.62 (-0.28)	4.99	4.98 (0.00)	SC (0.810)
H_2	0.11	2.38	0.75 (0.76)	0.69 (-0.16)	4.99	4.98 (0.00)	SC (0.652)
CH_4	0.13	2.54	1.10 (1.10)	0.72 (C: 0.67, H: -0.88)	5.00	4.99 (0.00)	SC (0.708)

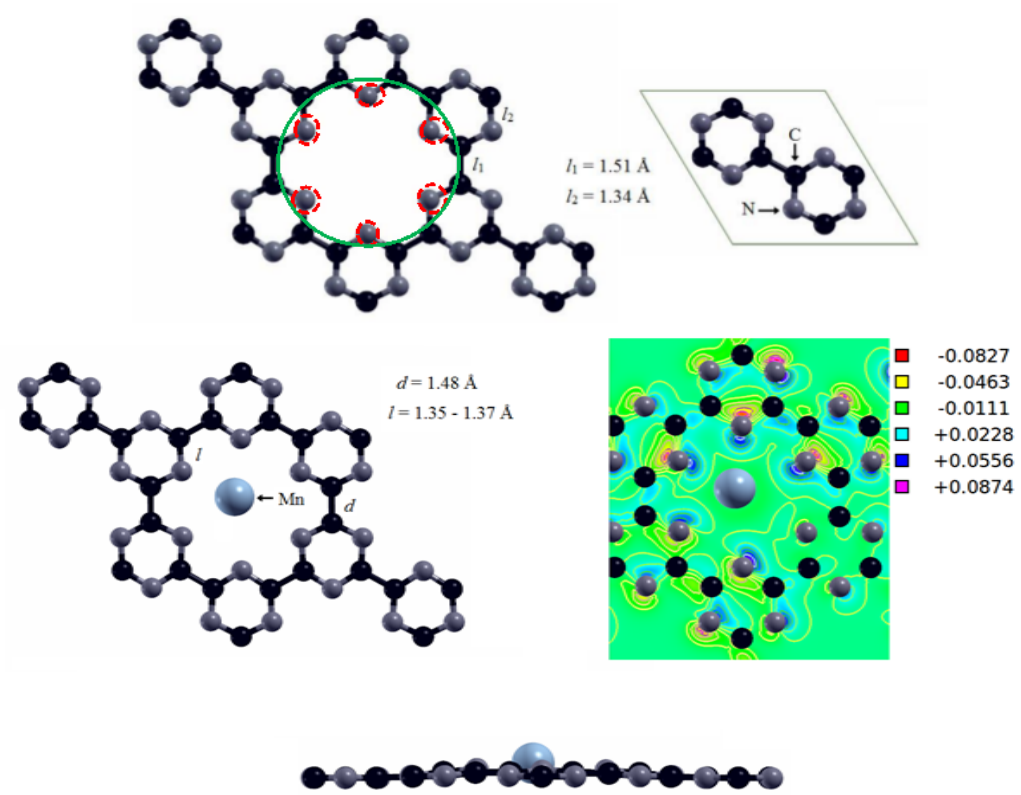

Figure 1 (a) **Left**: Top view of the optimized 2×2 geometry of C_6N_6. The atomic symbols and the calculated bond leghts are shown in the figure. Atoms in dotted red circles are the edge nitrogen atoms (N_{edge}). There are N_{edge}=6 of them around the cavity. **Right**: unit cell of *s*-triazine which is made of 2 C_3N_3 rings. (b). Left: Top view of a supercell comprised of 2×2 *s*-triazine unit cell, with an embedded Mn atom (Mn-C_6N_6). This Mn-C_6N_6 is the one that was used as the input in our calculation. **Right**: Top view plot of the charge-density difference of the Mn atom and the surrounding C and N atoms. The color scale shows ranges of charge accumulation and depletion in a.u. Carbon atoms are in black. Atoms dotted with 4-point starts are the N_{edge} atoms (nitrogen atoms in dark ash color). **Down**: Side view of the optimized buckled Mn-C_6N_6 under applied perpendicular electric field.

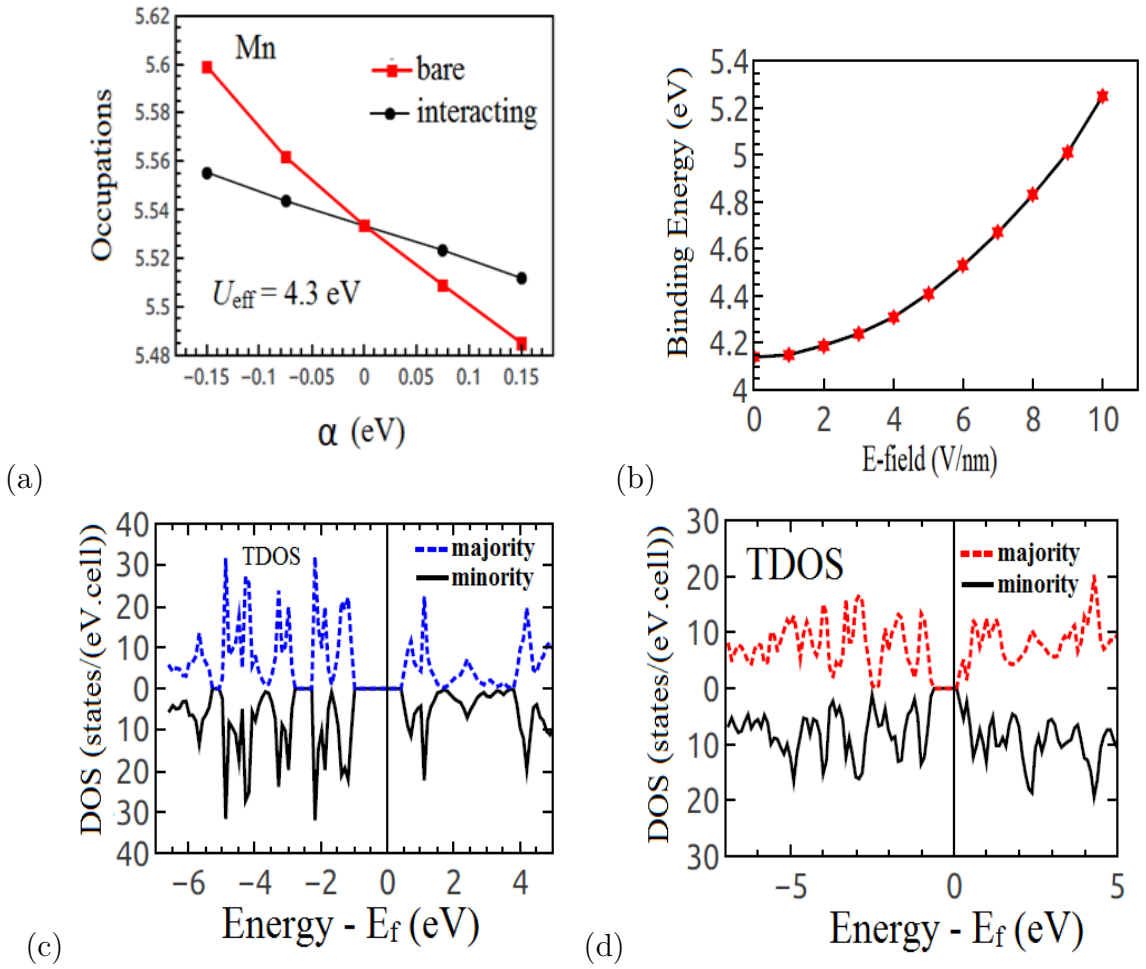

Figure 2 (a) **Left**: Linear response of d orbital occupations as a function of potential shift α. The curves depicted by the dotted red and black lines are labeled bare and interacting. The inverse response functions are deduced numerically by calculating the slope of the curves. χ_0 follows from the slope of curve bare, whereas χ from the slope of curve interacting. **Right**: The magnetic moment per unit cell and binding energy depicted by the dotted red and black lines respectively as a function of an applied electric field for Mn-C_6N_6 system. **Down**: The spin-polarized total density of state (TDOS) for Mn-C_6N_6 under applied electric field.

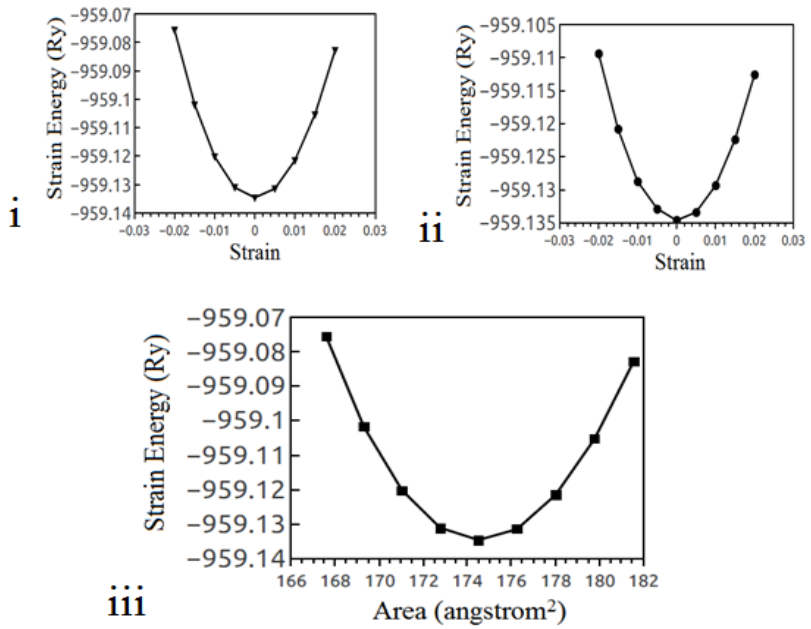

Figure 3 Dependence of strain energy (Ry) on (i) bi-axial (ii) uni-axial and (iii) area of the Mn-C_6N_6 system for elastic constant calculation.

*[!p]

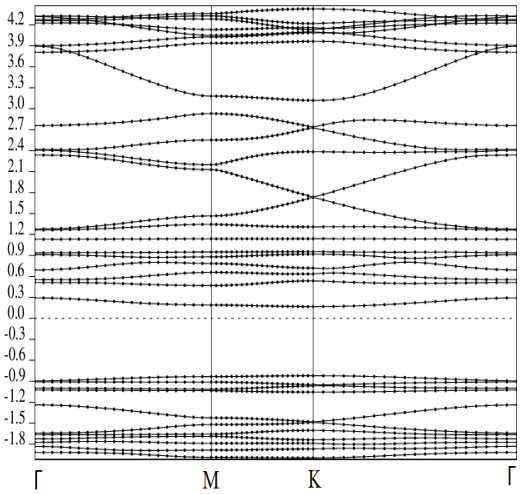
Γ
M
K
Γ

(a)

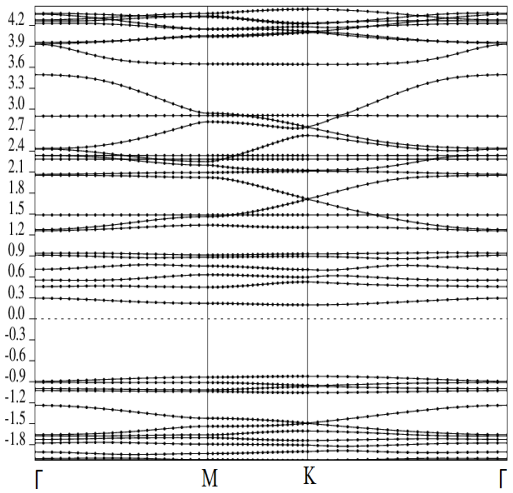
Γ
M
K
Γ

(b)

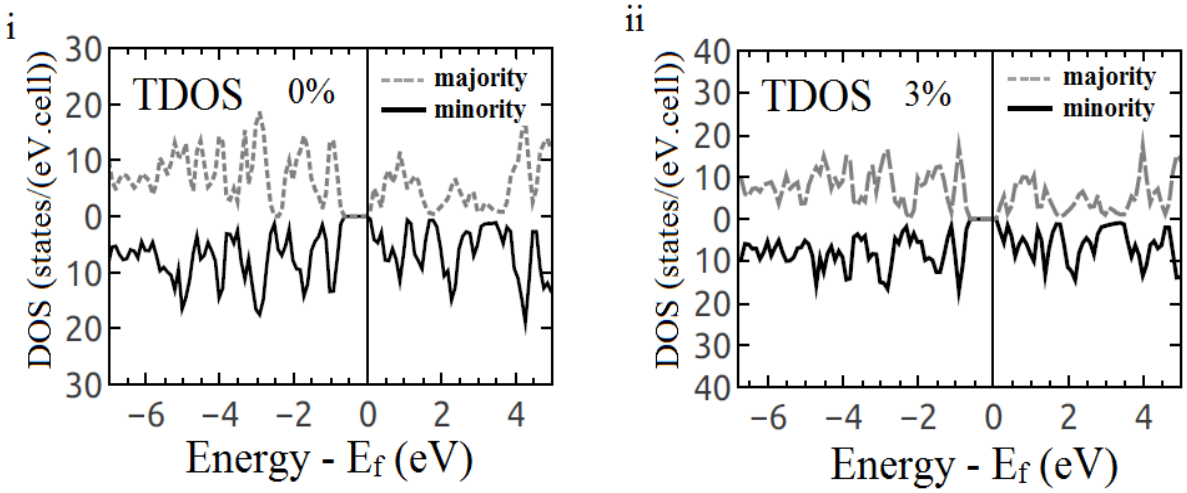
i
TDOS 0%
majority
minority
DOS (states/(eV.cell))
Energy - Ef (eV)
ii
TDOS 3%
majority
minority
DOS (states/(eV.cell))
Energy - Ef (eV)

(c)

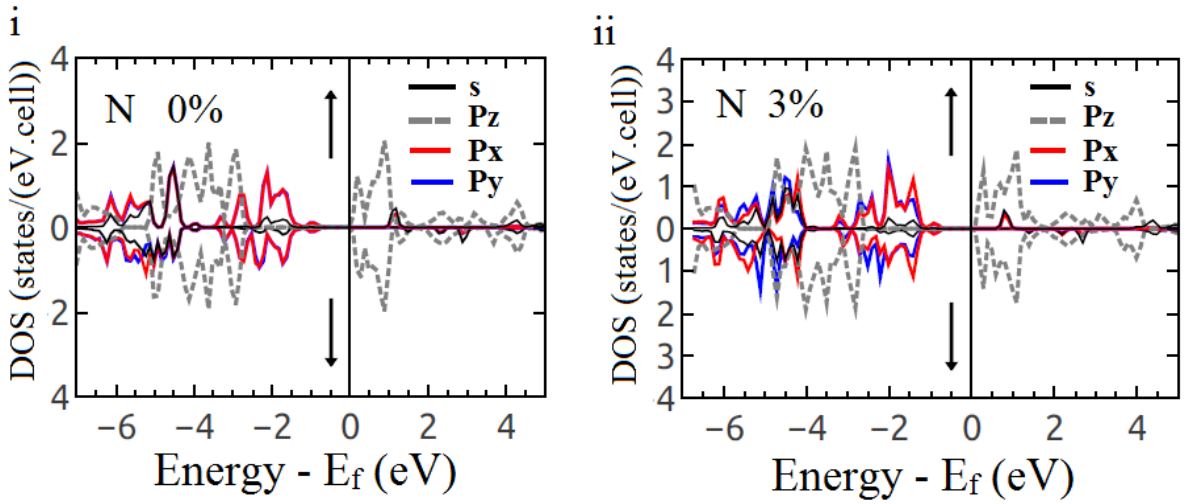
i
N 0%
s
Pz
Px
Py
DOS (states/(eV.cell))
Energy - Ef (eV)
ii
N 3%
s
Pz
Px
Py
DOS (states/(eV.cell))
Energy - Ef (eV)

(d)

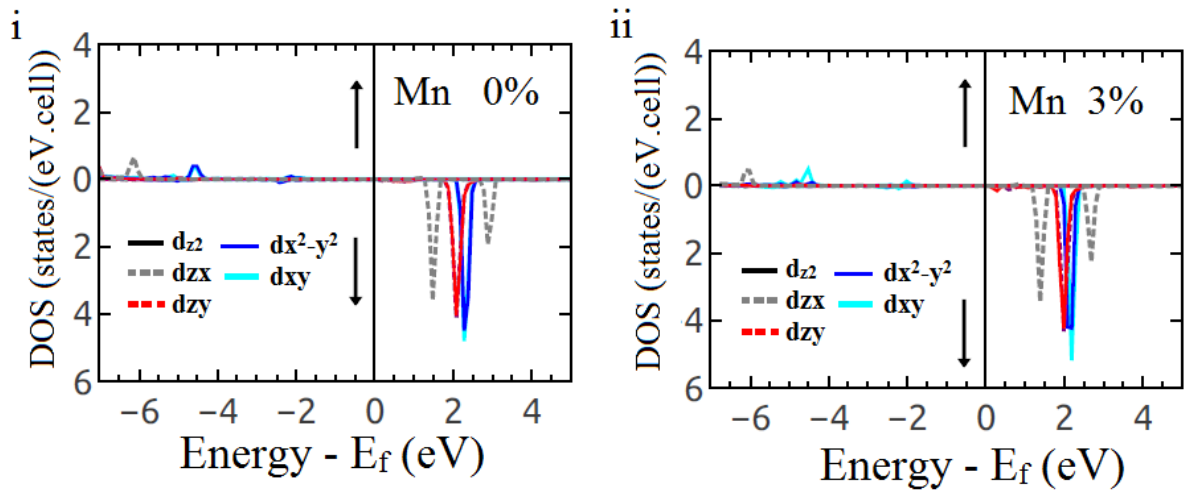

(e)

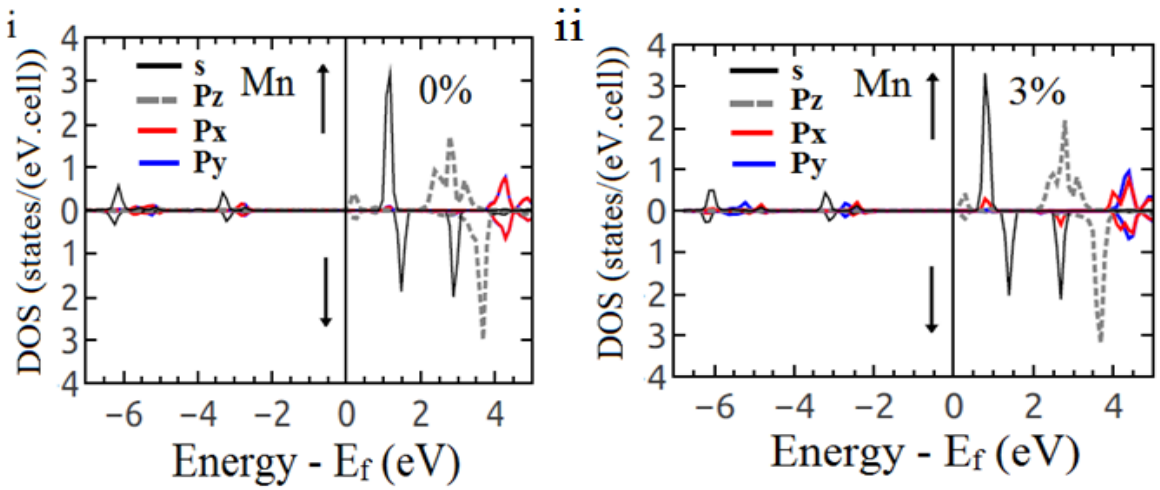

(f)

Figure 4 Spin-polarized electronic band structure (a) majority (b) minority spin states for unstrained ($s = 0$) Mn-C_6N_6 system. Spin-polarized TDOS and projected density of state (PDOS) for strain-free (b)i-(f)I and strained (b)ii-(f)ii systems respectively.

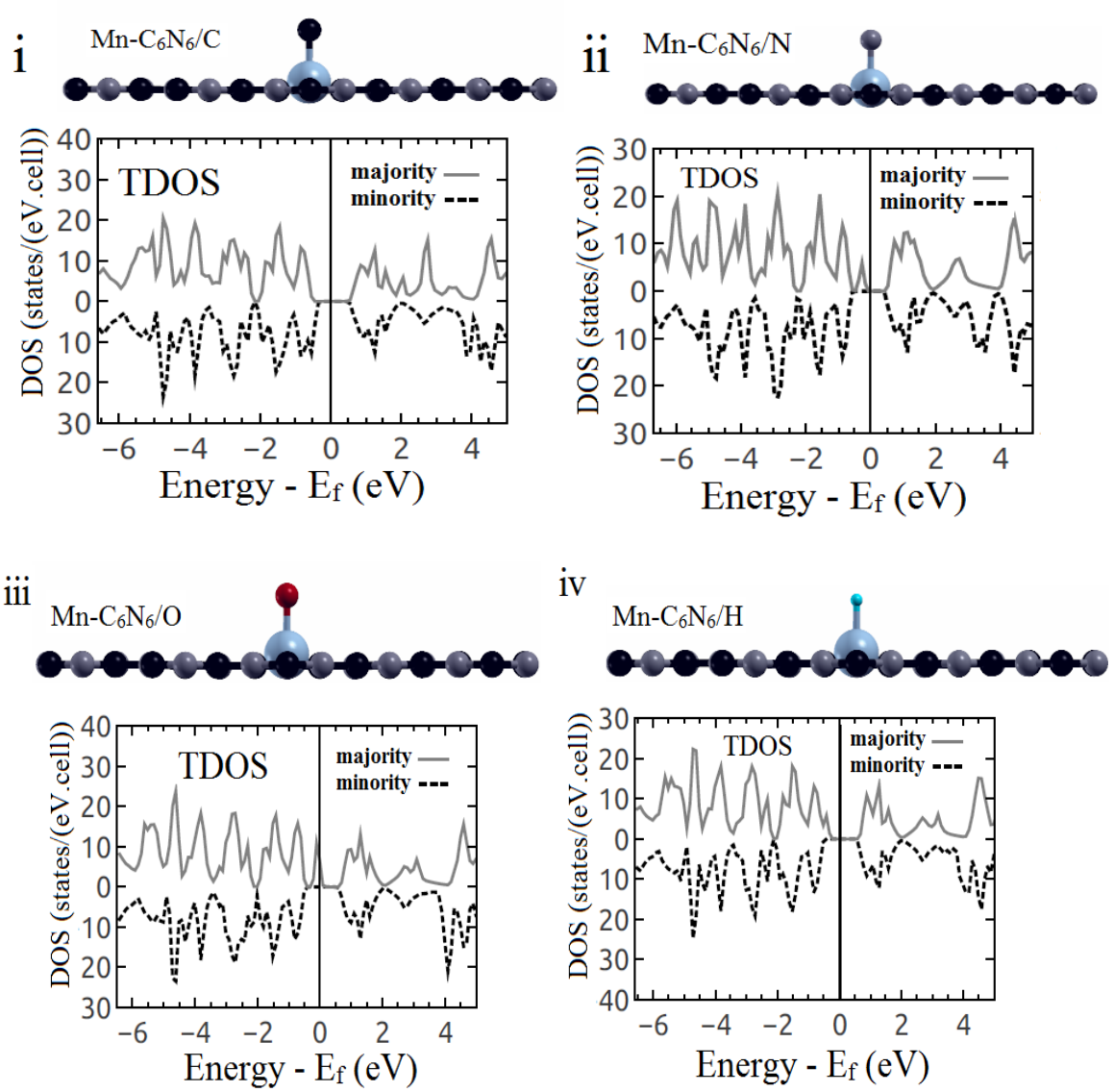

Figure 5 Spin-polarized TDOS and side view for Mn-C_6N_6 with an adsorbed (i) C (ii) N (iii) O and (iv) H atoms.

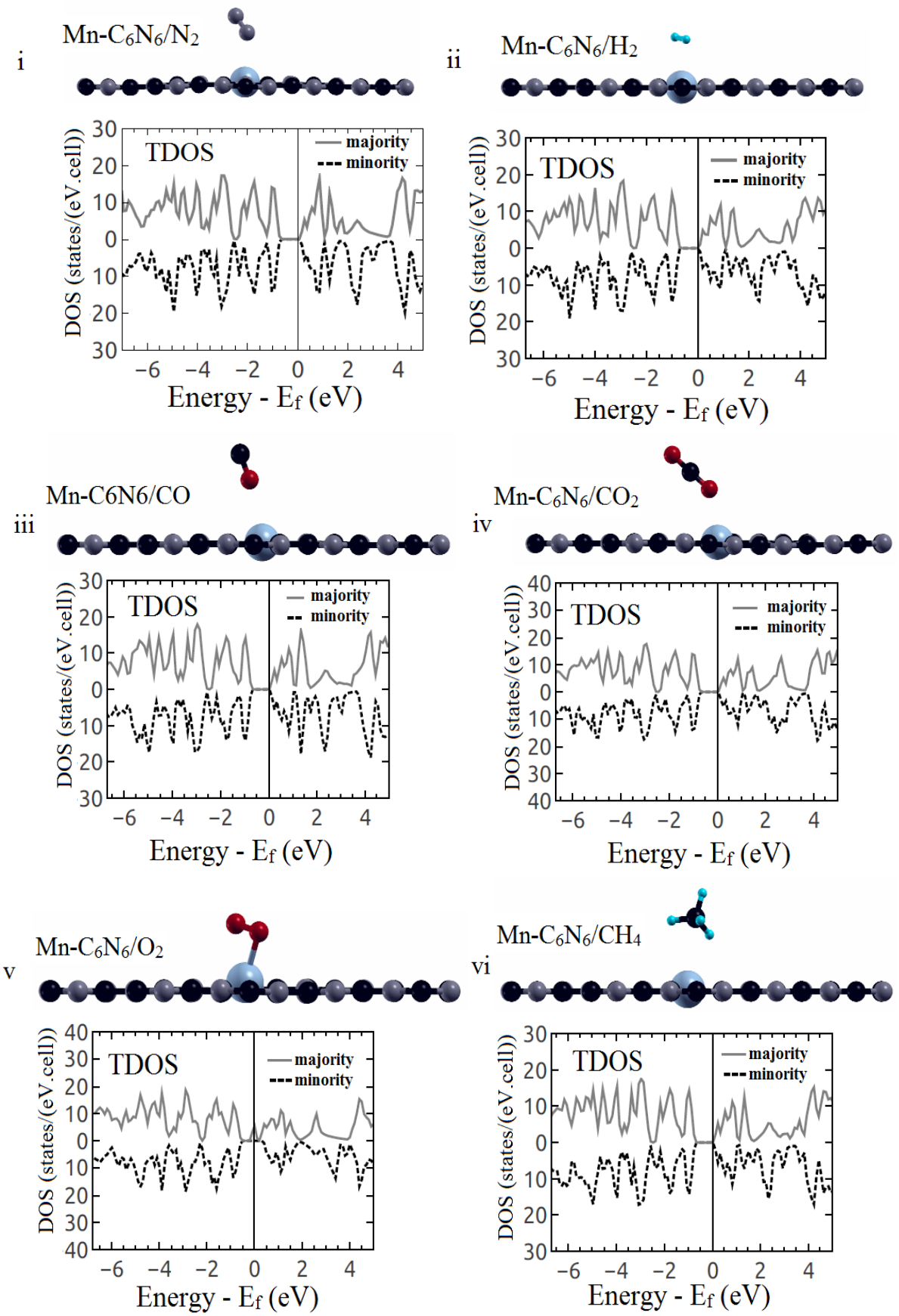

Figure 6 Spin-polarized TDOS and side view for Mn-C_6N_6 with an adsorbed (i) N_2 (ii) H_2 (iii) CO (iv) CO_2 (v) O_2 and (vi) CH_4 molecules.